Partial discharge detection based on Rydberg-atom electric field sensing

En-Hui Wang(王恩惠), Qi-Feng Wang(王启锋), Jia-Qi Geng(耿佳琪), Teng Tian(田腾), Ru-Jia Qiu(仇茹嘉), Bing Xue(薛冰), Yi-Wei Yuan(袁一玮), Long Zhao(赵龙), Dong-Sheng Ding(丁冬生)
Citation: Chin. Phys. B. 35, 104209 (2026). DOI: 10.1088/1674-1056/ae306e | CSTR: 32038.14.CPB.ae306e
http://cpb.iphy.ac.cn; http://iopscience.iop.org/cpb

What follows is a list of articles you may be interested in

Transfer of Fisher information in quantum postselection metrology

Zi-Rui Zhong(钟子瑞), Ke-Xuan Chen(陈可轩), Xia-Lin Su(苏夏临), Hui-Lin Xu(徐惠林), Yan Zhang(张妍), Xiang-Ming Hu(胡响明), Qing-Lin Wu(吴青林)
Chin. Phys. B. 35, 074203 (2026). DOI: 10.1088/1674-1056/ae194f | CSTR: 32038.14.CPB.ae194f

Sensitive sensing based on quantum correlation of photons in weak nonlinear regime

Zi-Qiang Yin(尹子强), Zhi-Hao Liu(刘志豪), Jian Tang(唐健), Hui Jing(景辉), Xun-Wei Xu(徐勋卫)
Chin. Phys. B. 35, 074201 (2026). DOI: 10.1088/1674-1056/ae5c71 | CSTR: 32038.14.CPB.ae5c71

Generation of squeezed states of magnons and photons based on the Kerr effect in cavity-magnon hybrid system

Cheng-Hua Bai(白成华), Suying Bai(白素英)
Chin. Phys. B. 35, 044210 (2026). DOI: 10.1088/1674-1056/ae4b2d | CSTR: 32038.14.CPB.ae4b2d

Super-resolving refractive index measurements with even coherent-state sources and parity detection

Qiang Wang(王强), Xiaohao Yang(杨晓豪), Fu Song(宋甫), Lili Hao(郝利丽)
Chin. Phys. B. 34, 124202 (2025). DOI: 10.1088/1674-1056/ade8de | CSTR: 32038.14.CPB.ade8de

Quasi-two-dimensional isotropic laser cooling of atoms for quantum sensing

Xiao Zhang(张孝), Yi Song(宋屹), Yuan Sun(孙远), Liang Liu(刘亮)
Chin. Phys. B. 34, 084202 (2025). DOI: 10.1088/1674-1056/add4f7 | CSTR: 32038.14.CPB.add4f7

Partial discharge detection based on Rydberg-atom electric field sensing

En-Hui Wang(王恩惠)[1,†,‡], Qi-Feng Wang(王启锋)[2,†], Jia-Qi Geng(耿佳琪)[1], Teng Tian(田腾)[1], Ru-Jia Qiu(仇茹嘉)[1], Bing Xue(薛冰)[1], Yi-Wei Yuan(袁一玮)[1], Long Zhao(赵龙)[1], and Dong-Sheng Ding(丁冬生)[2,§]

[1] *State Grid Anhui Electric Power Research Institute, Hefei* 230601, *China*
[2] *Key Laboratory of Quantum Information, University of Science and Technology of China, Hefei* 230026, *China*

(Received 16 November 2025; revised manuscript received 21 December 2025; accepted manuscript online 23 December 2025)

Partial discharge (PD) detection has garnered considerable attention due to its critical role in condition assessment and fault prediction of power system equipment. However, efficient and accurate acquisition of PD signals remains a significant technical challenge. Among mainstream technologies, the ultra-high frequency (UHF) detection method plays a key role in capturing PD signals. This work introduces a Rydberg atom-based electric field sensing approach for PD detection, employing a three-photon excitation scheme in cesium vapor. Four representative PD types are investigated: void, floating, particle, and corona, revealing the ability of the nonmetallic atomic sensor to capture their distinct time-domain characteristics and periodic behaviors at the power frequency. In addition, an antenna–waveguide–vapor cell coupling configuration is proposed. This electro-optical to opto-electronic conversion mechanism allows the sensor to achieve long-range detection while preserving favorable signal-to-noise ratios. Although the sensor's limited instantaneous bandwidth leads to pulse broadening in high-speed signals, its theoretical high sensitivity and wide operating bandwidth highlight its potential as a complement to traditional metal-antenna solutions. These findings provide a robust foundation for implementing quantum-enhanced PD monitoring in practical power engineering scenarios.

Keywords: quantum measurement, Rydberg atom, electrical power system, radio frequency

PACS: 42.50.Dv, 32.80.Ee, 84.70.+p, 84.40.–x

DOI: 10.1088/1674-1056/ae306e **CSTR:** 32038.14.CPB.ae306e

1. Introduction

Partial discharge (PD) detection is critical for ensuring the insulation integrity and operational reliability of high-voltage electrical equipment. PD refers to a localized dielectric breakdown that occurs within insulating materials subjected to high-voltage stress, which can lead to insulation aging and eventual equipment failure; thus, early detection is of significant importance.[1,2] Existing PD detection methods mainly include electrical pulse, acoustic, chemical, optical, and electromagnetic techniques.[3–7] Among these methods, ultra-high frequency (UHF, 0.3 GHz to 3 GHz) electromagnetic detection technology has received widespread attention and is widely used for PD monitoring in high-voltage electrical equipment. Its advantages of non-intrusive, non-contact measurement, high sensitivity, and a strong signal-to-noise ratio make it a vital method for assessing insulation conditions in power systems.[8,9]

Traditional UHF detection typically utilizes metallic antennas to capture electromagnetic waves in the GHz range generated by PD, subsequently achieving online monitoring through signal processing equipment.[10,11] However, metallic antennas exhibit several inherent limitations; specifically, they are susceptible to electrical breakdown under intense electric fields, potentially damaging sensors, and propagating faults to expensive downstream data acquisition and analysis systems. Additionally, metallic antennas typically feature complex structures and considerable size, complicating portable implementations.[12,13]

In recent years, rapid advances in quantum sensing technology have offered novel approaches to electric field detection. Electric field sensors based on Rydberg atoms have emerged as promising alternatives to conventional metallic antennas due to their superior theoretical sensitivity and broadband frequency response.[14–23] Rydberg atoms, which are highly excited neutral atoms with outermost electron states that are extremely sensitive to external electric fields, enable precise measurements of the electric field strength and frequency via laser spectroscopy of shifts in atomic energy levels.[24–28] Compared with traditional metallic antennas, quantum sensors exhibit an ultra-wideband response ranging from DC to the terahertz regime and theoretical detection sensitivities far exceeding the physical limits of metallic antennas at room temperature. Moreover, their purely optical measure-

[†]These authors contributed equally to this work.
[‡]Corresponding author. E-mail: enhuiwang@ustc.edu.cn
[§]Corresponding author. E-mail: dds@ustc.edu.cn

© 2026 Chinese Physical Society and IOP Publishing Ltd. All rights, including for text and data mining, AI training, and similar technologies, are reserved.

ment methodology eliminates the risk of electrical breakdown inherent in metallic probes, leading to simpler sensor structures and facilitating miniaturization.[29–34]

In this study, we investigate the response characteristics of Rydberg atom-based electric field sensors to four typical types of PD radio-frequency (RF) signals. In the experiments, a three-photon excitation scheme for cesium Rydberg atoms is constructed, enabling the detection of RF signals generated by professional PD equipment, including void discharge, floating discharge, particle discharge, and corona discharge. A detailed time-domain analysis of the experimental results is performed. The core component of the atomic sensor is a high-voltage-resistant, non-metallic glass gas cell. The antenna–waveguide–gas cell coupling configuration provides an electro-optic to opto-electric conversion mechanism, which effectively protects the downstream equipment during PD detection. Finally, the causes of signal distortion during atomic detection are discussed.

2. Experiment setup

In this experiment, a three-photon excitation scheme is employed to excite ground-state cesium atoms to a high principal quantum number Rydberg state, as illustrated in Fig. 1(a). This scheme involves three resonant transitions among four atomic states of cesium, driven by lasers of different wavelengths. The probe laser (852 nm, DL PRO, TOPTICA) drives the transition between the ground state $6S_{1/2}$ and the first intermediate state $6P_{3/2}$. The dressing laser (1470 nm, DL 100, TOPTICA) drives the transition from $6P_{3/2}$ to the second intermediate state $7S_{1/2}$. The coupling laser (780 nm, TA PRO, TOPTICA) drives the transition from $7S_{1/2}$ to the Rydberg state $49P_{3/2}$. Furthermore, the three lasers are frequency-locked using saturated absorption spectroscopy, two-photon EIT spectroscopy, and three-photon EIT spectroscopy, respectively.

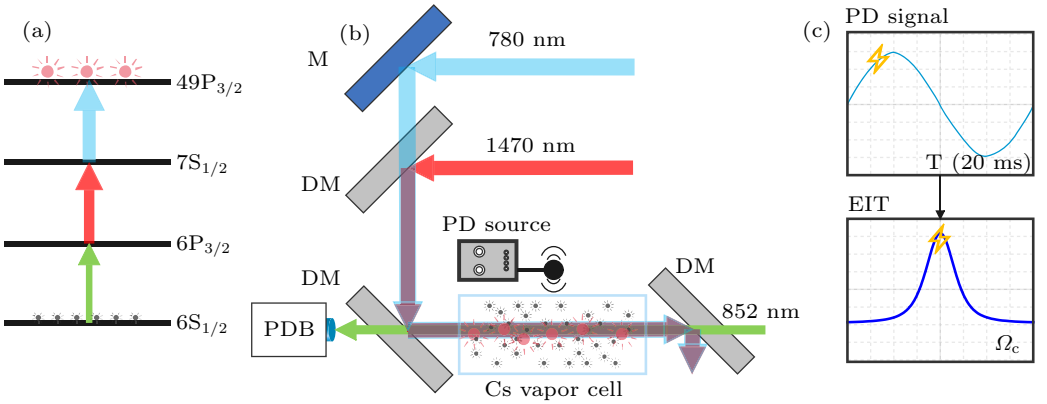

Fig. 1. (a) Energy-level diagram showing the excitation pathway from the ground state to the Rydberg state in cesium atoms. $6S_{1/2}$ denotes the ground state, $6P_{3/2}$ the first intermediate state, $7S_{1/2}$ the second intermediate state, and $49P_{3/2}$ the target Rydberg state. The corresponding excitation laser wavelengths are 852 nm, 1470 nm, and 780 nm, respectively. Black dots within the cesium vapor cell represent cesium atoms in the ground state, while red dots indicate atoms excited to the Rydberg state. (b) Experimental optical setup illustrating the three-photon excitation scheme used to excite cesium atoms from the ground state to Rydberg states. In the diagram, M denotes mirror, DM denotes dichroic mirrors, and PDB denotes a balanced photodetector. The green beam indicates the probe laser at 852 nm, the red beam represents the dressing laser at 1470 nm, and the light blue beam corresponds to the coupling laser at 780 nm. (c) Schematic of the spectral readout principle for PD signals. The perturbation of Rydberg atoms by PD signals is probed via electromagnetically induced transparency spectroscopy.

The probe laser propagates horizontally through the cesium vapor cell, and the transmitted signal is detected by a PDB (PDB450A-AC, Thorlabs) as shown in Fig. 1(b). The cesium vapor cell measures $5 \times 1 \times 1$ cm^3. The dressing laser and coupling laser are combined using a DM and introduced into the vapor cell in a counter-propagating configuration with respect to the probe beam. Within the region where all three beams overlap, cesium atoms are sequentially excited from the ground state to Rydberg states. The probe, dressing, and coupling beams exhibit waist radii and Rabi frequencies of $w_p \approx 200$ μm, $\Omega_p \approx 2\pi \times 75$ MHz; $w_d \approx 500$ μm, $\Omega_d \approx 2\pi \times 270$ MHz; $w_c \approx 500$ μm, $\Omega_c \approx 2\pi \times 5$ MHz. Due to their extremely high polarizability, Rydberg atoms are highly sensitive to external electric fields. This property provides the physical basis for electric field sensing and precise manipulation, constituting the core mechanism for RF signal reception and analysis in this study.

We achieve spectral readout of cesium Rydberg atoms in response to PD RF signals using electromagnetically induced transparency (EIT) in a three-photon excitation scheme, as illustrated in Fig. 1(c). In the experimental setup, cesium atoms are excited to high-principal-quantum-number Rydberg states and coupled to externally applied PD RF fields via off-resonant dipole interactions. This interaction induces significant modulations of the EIT transmission spectrum, thereby yielding a measurable optical signal for RF field sensing. The transmitted probe light is collected by a photodetector and recorded in the time domain using a high-speed oscilloscope, enabling indirect acquisition of the Rydberg atoms' dynamic response to the applied RF fields. The underlying physical

mechanism is attributed to the AC Stark effect,[35] which describes the frequency-dependent energy level shifts of atoms in oscillating external electric fields. For non-resonant fields far detuned from atomic transitions, the energy shift is primarily governed by second-order perturbation theory and can be expressed as

$$\Delta E = -\frac{1}{4}\alpha(\omega)E^2,$$

where ΔE is the energy level shift, $\alpha(\omega)$ denotes the dynamic polarizability at angular frequency ω, and E is the amplitude of the external electric field. When the electric field comprises multiple frequency components, i.e., a composite RF signal, it can be written in the time domain as

$$E(t) = \sum_i E_i \cos(\omega_i t + \phi_i),$$

where E_i, ω_i, and ϕ_i represent the amplitude, angular frequency, and initial phase of the ith component, respectively.

3. Results and discussion

To enable the detection of PD RF signals using a Rydberg atom-based sensor, two RF signal coupling schemes are developed, as illustrated in Fig. 2(a). The first scheme (test 2) is a free-space coupling configuration, in which the PD signal source is placed about 5 cm away from the cesium vapor cell. RF signals propagate directly through free space and interact with Rydberg atoms inside the cell. This setup has a simple structure, which facilitates straightforward experimental assembly and alignment, and effectively demonstrates the direct response of Rydberg atoms to externally applied electric fields in an open environment. The second scheme (test 3) is a waveguide-enhanced coupling configuration.[36,37] In this setup, the PD signal source is also positioned about 5 cm from an Archimedean spiral antenna. The emitted RF signal is first received by the antenna and then transmitted via a 5-m coaxial cable to an integrated waveguide chip mounted on the surface of the cesium vapor cell. This configuration generates a locally enhanced electric field at the cell interface, enabling efficient coupling with the Rydberg atoms.

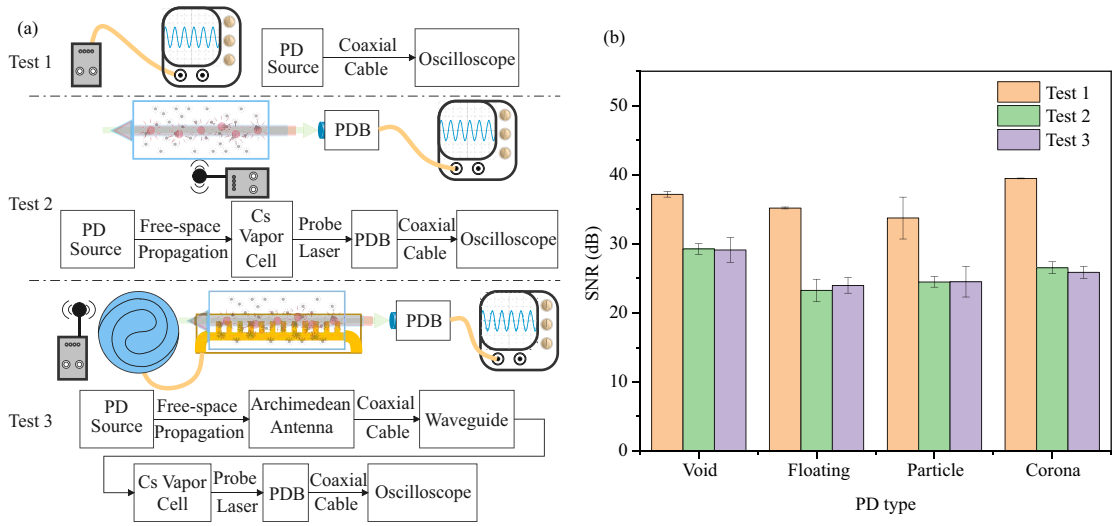

Fig. 2. (a) Schematic and block diagrams of three acquisition pathways for PD RF signals. Scheme 1 (test 1) records raw PD RF signals directly with an oscilloscope. Scheme 2 (test 2) couples the PD signals into the atomic sensing system via free-space propagation. Scheme 3 (test 3) receives the PD signals with an Archimedean spiral antenna, routes them through a coaxial cable, and couples them to the atomic system through a waveguide. (b) Comparison of power signal-to-noise ratio (power SNR) for four canonical PD types — void, floating, particle, and corona — under the three reception schemes in (a). The horizontal axis lists the PD types; the vertical axis reports the corresponding SNR. These results clearly show that the choice of reception and coupling pathway materially affects the sensing performance of the atomic system.

The PD source employed in this experiment is the JD-CL20 model, a professional PD signal generator developed by JuDian-Electric. This device generates nanosecond-scale UHF pulse signals and can effectively simulate common PD types, such as void, floating, particle, and corona discharges. The signals are emitted through an integrated rod antenna or via a standard SMA connector for wired transmission. The Archimedean spiral antenna used in the experiment is fabricated on a printed circuit board with a diameter of 30 cm and demonstrates broadband performance. Its operational frequency range extends from 100 MHz to 6 GHz, covering the primary RF spectrum associated with PD signals.

Due to the requirement for tight integration of Rydberg atomic vapor cells with complex optical systems, achieving in-situ, close-proximity detection of PD sources remains challenging in practical engineering environments. To improve the applicability and deployment flexibility of Rydberg atom-based systems, test 3 proposes a novel signal coupling scheme, which combines a spiral antenna with a waveguide structure. This design efficiently couples remotely received PD RF signals into the atomic system, enabling stable optical readout. Figure 2(b) presents experimental results comparing

the signal-to-noise ratio (SNR) performance of three reception schemes: direct acquisition of raw PD RF signals (test 1), atomic detection via free-space coupling (test 2), and atomic detection using the proposed spiral antenna–waveguide coupling scheme (test 3).

The results show that raw PD signals retain high quality, with SNR values no lower than 33 dB. Although both atom-based detection methods exhibit signal attenuation, their SNRs remain above 23 dB and the variation among different test schemes for the same discharge type remains within 1 dB, showing comparable performance. Notably, the spiral antenna–waveguide coupling scheme extends the effective detection range from the centimeter scale typical of free-space coupling to the meter scale. Experimental validation confirms stable signal sensing at distances up to 5 meters via coaxial transmission. Moreover, this approach leverages an electro-optical to optoelectronic conversion mechanism, effectively eliminating the risk of electrical breakdown commonly associated with traditional UHF detection techniques. Converting RF signals into low-frequency optical outputs, the atomic system also significantly reduces hardware complexity in the signal acquisition and processing chain, eliminating the need for high-speed, high-performance electronic components. This method offers a practical and scalable pathway for deploying atomic RF sensing technology in real-world engineering applications.

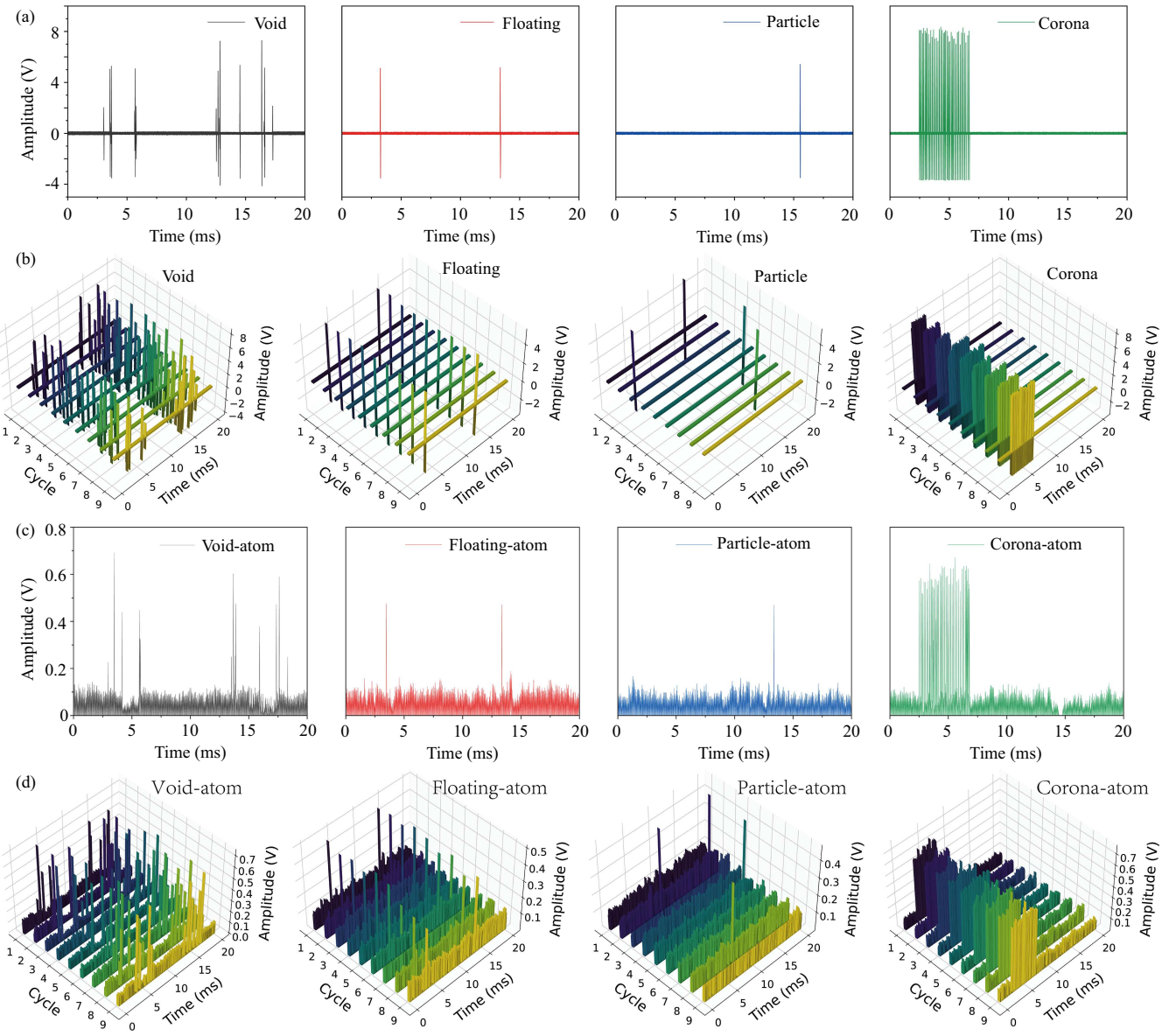

Fig. 3. Time-domain waveforms of RF signals. (a) The 2D plot shows the time-domain characteristics of raw signals emitted by a PD source within a single power-frequency cycle, corresponding to four typical discharge types: void, floating, particle, and corona discharges. (b) The 3D plot illustrates the periodic time-domain characteristics of raw signals from the PD source over multiple power-frequency cycles. (c) The 2D plot presents the time-domain characteristics of PD signals received by the atomic system within a single power-frequency cycle. (d) The 3D plot displays the periodic time-domain characteristics of PD signals received by the atomic system over multiple power-frequency cycles. Measurements in (a), (b) correspond to test 1, and those in (c), (d) correspond to test 2. Each dataset shown represents an independent measurement performed separately.

To verify the accuracy of the PD signal reception results obtained from the atomic system, the PD signal source is directly connected to a high-bandwidth oscilloscope via a coaxial cable to obtain reference time-domain waveforms (test 1). The PD signal waveforms over a single power-frequency cycle are presented in Fig. 3(a). Each of the four typical PD types exhibits characteristic temporal distributions. The void discharge exhibits two distinct clusters occurring on either side of the voltage peaks in both the positive and negative half-cycles of the AC waveform. The floating discharge exhibits two isolated single pulses. Their phases correspond to the latter part of the voltage rise at one-quarter and three-quarters of the cycle. The particle discharge is characterized by a single pulse near the voltage peak of the negative half-cycle. The corona discharge exhibits a pronounced cluster near the voltage peak of the positive half-cycle. The three-dimensional time-domain characteristics of PDs over multiple cycles are shown in Fig. 3(b). The void, floating, and corona discharges exhibit pronounced periodic repeatability, with discharge pulses occurring at stable phases. In contrast, the particle discharge displays significant randomness, with single pulses appearing unpredictably in the time domain without a fixed phase.

Figures 3(c) and 3(d) present the time-domain response waveforms of the atomic system (test 2). The observed waveform features show strong agreement with those of the raw PD signals in Figs. 3(a) and 3(b). Specifically, void discharges exhibit two distinct clusters per cycle, floating discharges produce two isolated high-amplitude pulses — one in each half-cycle, particle discharges display highly random timing, and corona discharges occur predominantly during the positive half-cycle. These results demonstrate that the Rydberg atom-based RF electric field sensing system can effectively detect PD RF signals propagating through free space. Furthermore, it can accurately reconstruct their time-domain characteristics over the power-frequency cycle. The characteristic features of PDs received by the atomic system enable clear identification of different PD types. The excellent consistency between the atomic sensor and conventional high-bandwidth oscilloscope measurements further validates the capability and reliability of the atomic sensing approach.

Significant distortion in the atomic system's response is observed in a single-pulse analysis of the PD signal (illustrated by corona discharge). As shown in Fig. 4(a), the original corona-discharge signal exhibits a pulse width of approximately 200 ns and contains rich temporal features. In contrast, Fig. 4(b) shows the atomic system's response to a single corona-discharge pulse, where the pulse is markedly broadened to approximately 15 μs — greatly exceeding the timescale of the original signal — and the fine waveform details are no longer resolvable. To investigate the origin of this distortion, the frequency spectrum of the corona-discharge signal and the instantaneous bandwidth of the atomic system are measured, as shown in Figs. 4(c) and 4(d). In the frequency domain, the corona-discharge spectrum is broadband with a pronounced peak at $\sim$ 200 MHz. Beyond this point, the spectral power decays and approaches the noise floor of the spectrum analyzer near 5 GHz. The experimental results indicate a 3 dB instantaneous bandwidth of approximately 170 kHz, which is significantly lower than the 4 MHz bandwidth of the photodetector. This discrepancy suggests that the distortion primarily arises from the limited bandwidth of the atomic system itself, which constrains its ability to accurately reconstruct the high-frequency components of the original PD signals. With further optimization, the instantaneous bandwidth of the Rydberg atomic system could be extended to the megahertz range;[38,39] however, for partial-discharge detection, the present system performance is already sufficient to meet the experimental requirements.

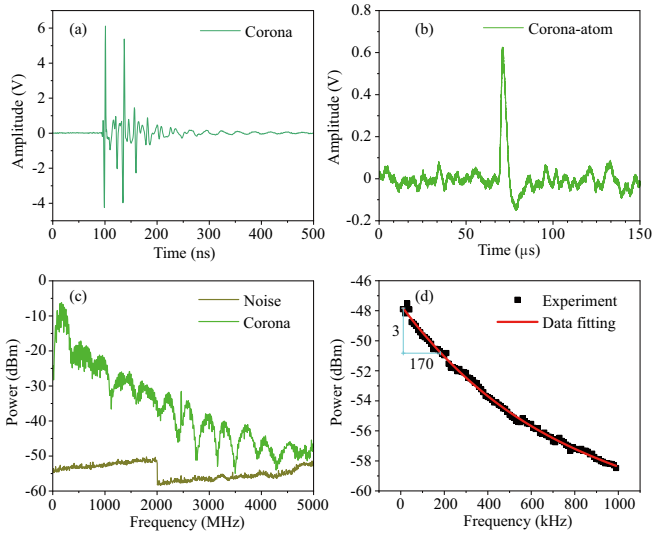

Fig. 4. (a) Raw oscilloscope trace of a single corona-discharge RF pulse (test 1), shown in the time domain. (b) Time-domain response waveform of the Rydberg atomic system to a single corona discharge pulse (test 2). It reveals the transient response characteristics of the atomic system to corona-type RF discharge signals. (c) The green curve corresponds to the frequency spectra of corona discharge signal, while the black curve represents the spectrum of background noise. (d) Measured instantaneous bandwidth of the atomic system. Black squares denote experimental data and the red curve is the fit. The 3 dB bandwidth, indicated in the panel, is approximately 170 kHz, demonstrating the system's capacity for transient RF response.

4. Conclusion

In conclusion, we demonstrate a Rydberg atom-based electric field sensing approach for the detection and analysis of RF signals generated by PDs. Using a three-photon excitation scheme and the EIT effect in cesium vapor, we successfully characterize the time-domain responses of Rydberg atoms to four typical PD types. Our experiments reveal that the atomic system can capture both the periodic and stochastic features of PD signals at power frequency, offering an optically accessible alternative to conventional UHF detection

techniques. Although the time-domain PD signals received by the atomic system exhibit some distortion, the system still demonstrates the capability to distinguish the four PD types. To address practical deployment challenges, we further propose and validate a spiral antenna–waveguide–vapor cell coupling configuration, which significantly extends the detection range while maintaining favorable SNR performance. These results highlight the potential of Rydberg atomic sensors as scalable, non-invasive, and electrically isolated solutions for future power system diagnostics and quantum-enhanced electromagnetic sensing applications.

Acknowledgements

We acknowledge funding from the Science and Technology Project of State Grid Anhui Electric Power Co., Ltd. (Project Number: B3120524001V), the National Key R and D Program of China (Grant No. 2022YFA1404002), and the National Natural Science Foundation of China (Grant No. T2495253).

References

[1] Al Saedi M A R and Yaacob M M 2014 *Adv. Mater. Res.* **845** 283
[2] Roslizan N, Rohani M, Wooi C, Isa M, Ismail B, Rosmi A and Mustafa W 2020 *J. Phys. Conf. Ser.* **1432** 012003
[3] Suo C, Zhao J, Wu X, Xu Z, Zhang W and He M 2023 *Electronics* **12** 336
[4] Ilkhechi H D and Samimi M H 2021 *IEEE Trans. Dielectr. Electr. Insul.* **28** 42
[5] Cheng H, Zeng F, Tang B, Li H, Tang J, Huang Z and Chao X 2023 *High Voltage* **8** 690
[6] Shen Z, Wang J and Wei G 2020 *Sensors* **20** 4767
[7] Boya C, Robles G, Parrado-Hernandez E and Ruiz-Llata M 2017 *Sensors* **17** 2625
[8] Azam S K, Othman M, Illias H A, Latef T A, Islam M T and Ain M F 2023 *Alexandria Eng. J.* **64** 709
[9] Chai H, Phung B T and Mitchell S 2019 *Sensors* **19** 1029
[10] Cui Z, Park S, Choo H and Jung K Y 2020 *Appl. Sci.* **10** 1698
[11] Liu J, Zhang G, Dong J and Wang J 2015 *Sensors* **15** 29434
[12] Gustafsson M, Sohl C and Kristensson G 2007 *Proc. R. Soc. A* **463** 2589
[13] Pfeiffer C 2017 *IEEE Trans. Antennas Propag.* **65** 1642
[14] Sedlacek J A, Schwettmann A, Kubler H, Low R, Pfau T and Shaffer J P 2012 *Nat. Phys.* **8** 819
[15] Fan H, Kumar S, Sedlacek J, Kubler H, Karimkashi S and Shaffer J P 2015 *J. Phys. B* **48** 202001
[16] Holloway C L, Gordon J A, Jefferts S, Schwarzkopf A, Anderson D A, Miller S A, Thaicharoen N and Raithel G 2014 *IEEE Trans. Antennas Propag.* **62** 6169
[17] Jing M, Hu Y, Ma J, Zhang H, Zhang L, Xiao L and Jia S 2020 *Nat. Phys.* **16** 911
[18] Fancher C T, Scherer D R, St John M C S and Marlow B L S 2021 *IEEE Trans. Quantum Eng.* **2** 3501313
[19] Simons M T, Artusio-Glimpse A B, Robinson A K, Prajapati N and Holloway C L 2021 *Measurement: Sensors* **18** 100273
[20] Liu B, Zhang L H, Liu Z K, Zhang Z Y, Zhu Z H, Gao W, Guo G C, Ding D S and Shi B S 2022 *Phys. Rev. Appl.* **18** 014045
[21] Yuan J, Yang W, Jing M, Zhang H, Jiao Y, Li W, Zhang L, Xiao L and Jia S 2023 *Rep. Prog. Phys.* **86** 106001
[22] Liu B, Zhang L, Liu Z, Deng Z, Ding D, Shi B and Guo G 2023 *Electromagnetic Science* **1** 1
[23] Wang Y J, Zhang J, Zhang Z Y, Shao S Y, Li Q, Chen H C, Ma Y, Han T Y, Wang Q F, Nan J D, *et al.* 2026 *Nat. Commun.* **17** 1160
[24] Li L, Jiao Y, Hu J, Li H, Shi M, Zhao J and Jia S 2023 *Opt. Express* **31** 29228
[25] Zhang H, Ma Y, Liao K, Yang W, Liu Z, Ding D, Yan H, Li W and Zhang L 2024 *Science Bulletin* **69** 1515
[26] Ding D S, Liu Z K, Shi B S, Guo G C, Molmer K and Adams C S 2022 *Nat. Phys.* **18** 1447
[27] Zhang L H, Liu Z K, Liu B, Zhang Z Y, Guo G C, Ding D S and Shi B S 2022 *Phys. Rev. Appl.* **18** 014033
[28] Zhang L, Liu Z, Liu B, Wang Q, Ma Y, Han T, Zhang Z, Chen H, Shao S, Li Q, *et al.* 2024 *Chin. Opt. Lett.* **22** 080201
[29] Liu B, Zhang L H, Wang Q F, Ma Y, Han T Y, Liu Z K, Zhang Z Y, Shao S Y, Zhang J, Li Q, *et al.* 2025 *Chin. Phys. Lett.* **42** 053201
[30] Kumar S, Fan H, Kubler H, Sheng J and Shaffer J P 2017 *Sci. Rep.* **7** 42981
[31] Simons M T, Gordon J A and Holloway C L 2018 *Appl. Opt.* **57** 6456
[32] Lin Y, Wu F C, Mao R Q, Yao J W, Liu Y, An Q and Fu Y Q 2022 *Acta Phys. Sin.* **71** 170702 (in Chinese)
[33] Meyer D H, Castillo Z A, Cox K C and Kunz P D 2020 *J. Phys. B* **53** 034001
[34] Wang Q F, Zhang L H, Liu B, Ma Y, Han T Y, Wang E H, Zhang Z Y, Shao S Y, Zhang J, Li Q, Chen H C, Wang Y J, Nan J D, Yin Y M, Ding D S and Shi B S 2025 *Phys. Rev. Appl.* **24** 014006
[35] Delone N B and Krainov V P 1999 *Phys.-Uspekhi* **42** 669
[36] Zhang L H, Liu B, Liu Z K, Zhang Z Y, Shao S Y, Wang Q F, Ma Y, Han T Y, Guo G C, Ding D S, *et al.* 2024 *Chip* **3** 100089
[37] Meyer D H, Kunz P D and Cox K C 2021 *Phys. Rev. Appl.* **15** 014053
[38] Hu J, Jiao Y, He Y, Zhang H, Zhang L, Zhao J and Jia S 2023 *EPJ Quantum Technol.* **10** 51
[39] Yan Y, Yang B, Li X, Zhao H, Yu B, Deng J, Chen L and Cheng H 2025 arXiv:2506.10541